Supplemental Information

Symbiotic Reactions over a High-Entropy Alloy Catalyst Enable Ultrahigh-Voltage Li–CO_2 Batteries

Experimental Procedure

Synthesis of Zn-DPCN Support

Zinc (II) nitrate hexahydrate (1.118 g; Beijing Tongguang Fine Chemical Company, AR) and 2-methylimidazole (1.232 g; Sigma-Aldrich, AR) were separately dissolved in methanol (Sigma-Aldrich, AR). After magnetic stirring for 30 min, the two solutions were combined and stirred at room temperature for 24 h. The resulting precipitate was collected by centrifugation, washed at least three times with methanol, and dried at 70 °C in a vacuum oven for 10 h to obtain the precursor, which was denoted as ZIF-8. Subsequently, ZIF-8 was heated at 900 °C in a tube furnace under Ar/H_2 (Hydrogen is 5wt%) flow for 3 h to obtain Zn-DPCN. This product was treated with 0.5 M H_2SO_4 for 1 h to remove unstable Zn. The sample was then washed until the pH was neutral, recovered by centrifugation, and dried to obtain the pretreated Zn-DPCN support.

Synthesis of PRZCNC-HEA Catalyst

First, 0.005 mmol of various nonprecious metals ($Co(acac)_2$ (Sigma-Aldrich, AR), $Ni(acac)_2$ (Sigma-Aldrich, AR), and $Cu(acac)_2$ (Sigma-Aldrich, AR)), and $Ru(acac)_3$ (Sigma-Aldrich, AR)) and $H_2PtCl_6 \cdot 6H_2O$ (0.6 mL of a 10 mM solution; Sigma-Aldrich, AR) were dissolved in 20 mL of a water and alcohol mixture. Next, the Zn-DPCN support (25 mg) was dispersed in this solution, which was then ultrasonicated for 30 min. To evaporate the solvent, the suspension was heated at 70 °C with magnetic stirring. The thick slurry was transferred to an oven and dried overnight. After grinding in an agate mortar, the powder was annealed and alloyed at 800 °C for 4 h under flowing Ar/H_2 (Hydrogen is 5wt%). After treatment with 0.1 M $HClO_4$ for 30 min, the mixture was centrifuged and dried overnight. Reference samples with different atomic ratios were synthesized using the same procedure.

Characterization

XRD patterns were recorded on a Bruker D8 Focus diffractometer at a scan rate of 1°

min^{-1} with Cu Kα radiation. TEM images were collected using a JEOL 2010F microscope operated at 200 kV. High-resolution STEM images, STEM-EDX mapping, and line scans were obtained using a Cs-corrected FEI Titan Themis Z microscope operated at 300 kV with a convergence semi-angle of 25 mrad and equipped a probe SCOR spherical aberration corrector. ICP-AES was performed using a Prodigy 7 ICP-AES instrument. The sample was pressed into a block for XRF analysis. XPS was performed using a VG ESCALAB MKII instrument with a Mg Kα X-ray source. The Ru, Co, Ni, Cu, and Zn K-edge spectra and Pt L_3-edge spectra were collected in fluorescence mode at beamline 1W2B with a Si (111) double-crystal monochromator at the Beijing Synchrotron Radiation Facility (BSRF). The ATHENA software package was used to analyze the XANES and EXAFS data.

Electrochemical Measurements

The catalyst was combined with PVDF as a binder at a weight ratio of 9:1 in *N*-methyl-2-pyrrolidone as a solvent to obtain a uniform slurry. This slurry was then applied to carbon cloth and dried under vacuum at 100 °C for 10 h. The resulting electrode had a mass loading of 1.0–2 mg cm^{-2}. Prototype Li–CO_2 batteries were assembled using CR2032-type coin cells with seven holes (Φ = 2 mm) in the cover for CO_2 diffusion. The electrolyte consisted of 1 M lithium bis(trifluoromethanesulfonyl)imide (LiTFSI) in tetraethylene glycol dimethyl ether (TEGDME). Lithium metal foil served as the anode and a Whatman A glass fiber separator was used to isolate the anode and cathode. The battery was assembled in a glovebox filled with high-purity argon, and electrochemical testing was carried out in a custom-made container.

Computational Details

All DFT calculations were implemented in the Vienna ab initio simulation package (VASP) using the projector-augmented wave (PAW) approach.[1,2] The HEA bulk structure was modeled using a special quasirandom structure (SQS) method with the sqsgenerator code.[3] Surface cleavage and site search modeling were performed within

the code based on pymatgen.[4] When constructing the slab models, a vacuum space of 15 Å was adopted to reduce the influence of adjacent images. Structural relaxation was performed via spin-polarized calculations and the generalized gradient approximation with the Perdew–Burke–Ernzerhof (PBE) functional. The energy cut-off of the plane waves was set to 500 eV. For all the calculations with slab models, a K-spacing value of 0.04 was used to generate K-Mesh.[5] bulk, surface, and adsorption model structures were fully relaxed using energy and force convergences of 1 10^{-5} eV and 0.02 eV $Å^{-1}$, respectively. The dispersion-corrected DFT-D3 method was used to describe the van der Waals (vdW) interactions.[5]

In Situ FTIR Investigation

A single-crystal silicon wafer with a gold coating was used as a substrate to enhance surface signals during in situ FTIR measurements. An in situ infrared test cell (HighSurrey) with a single-crystal Si window was used for all measurements. The electrochemical cell utilized springs to vary the load, ensuring close contact between the positive and negative electrodes and the separator. The optical table was equipped with an optical stage that had a continuously adjustable angle of incidence (30°–80°). After calibration, the angle was fixed at 60° with a surface penetration depth of 0.4–46 μm. The scanning range was 600–4000 cm^{-1}. During charge–discharge, signals were acquired every 60 mAh g^{-1}.

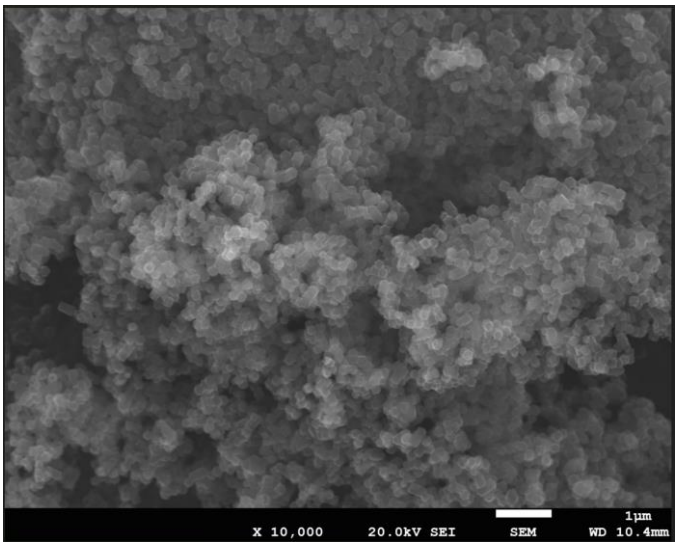

Figure S1. SEM image of Zn-DPCN.

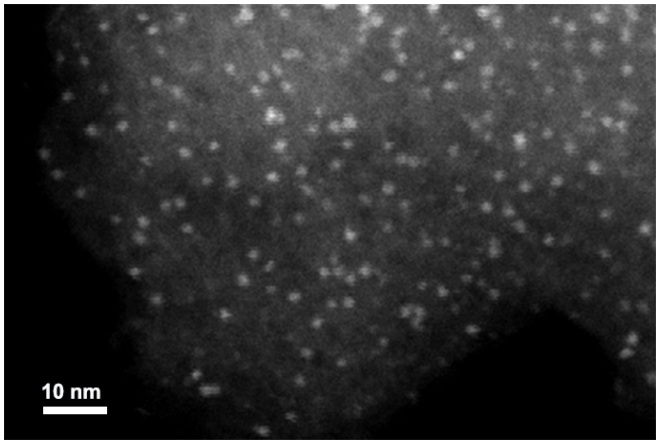

Figure S2. TEM image of PRZCNC-HEA.

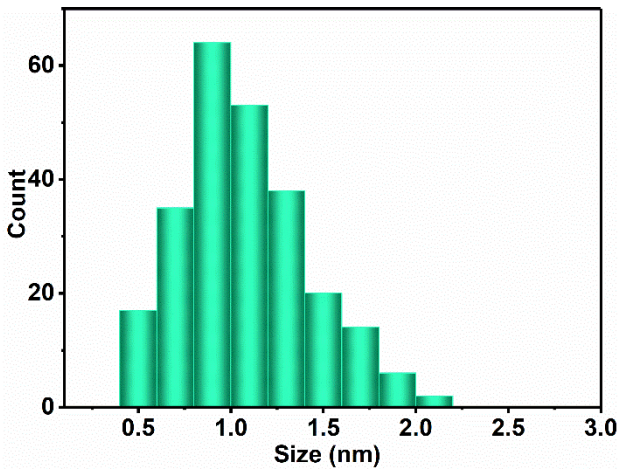

Figure S3. Particle size distribution histogram of PRZCNC-HEA.

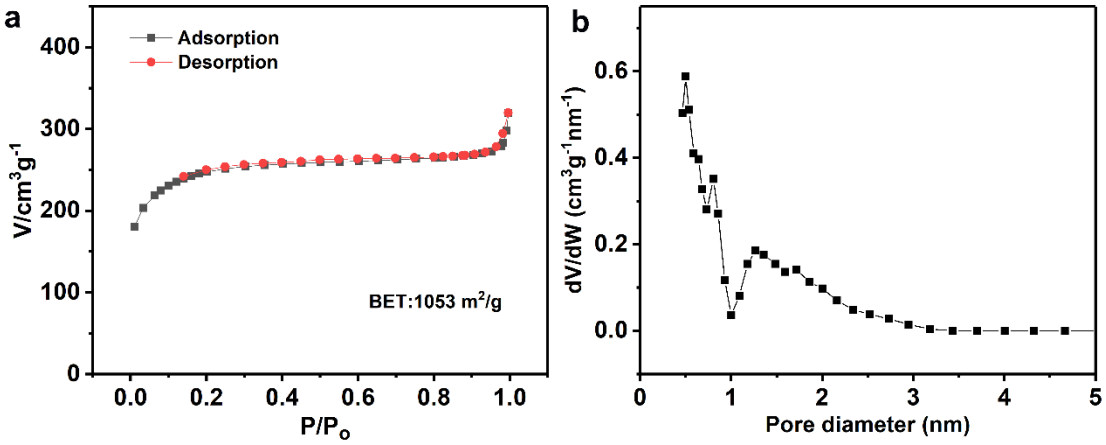

Figure S4. (a) N_2 adsorption–desorption isotherm and (b) pore size distribution of PRZCNC-HEA.

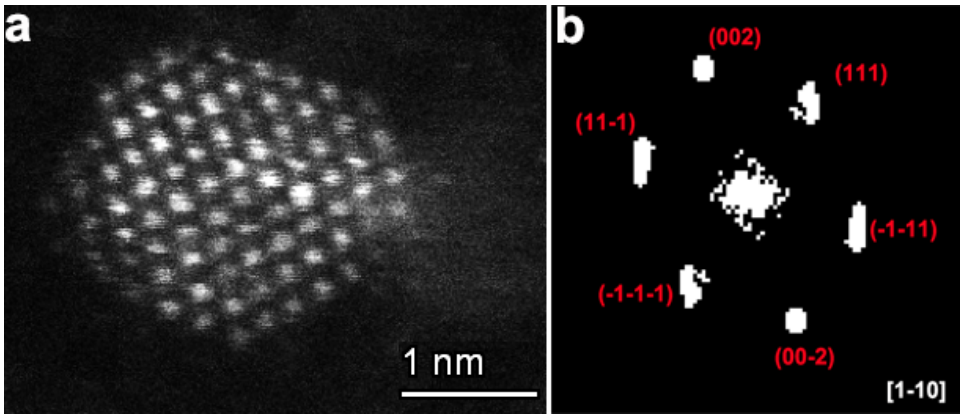

Figure S5. (a) HAADF-STEM image of PRZCNC-HEA and (b) corresponding Fourier transform electron diffraction pattern.

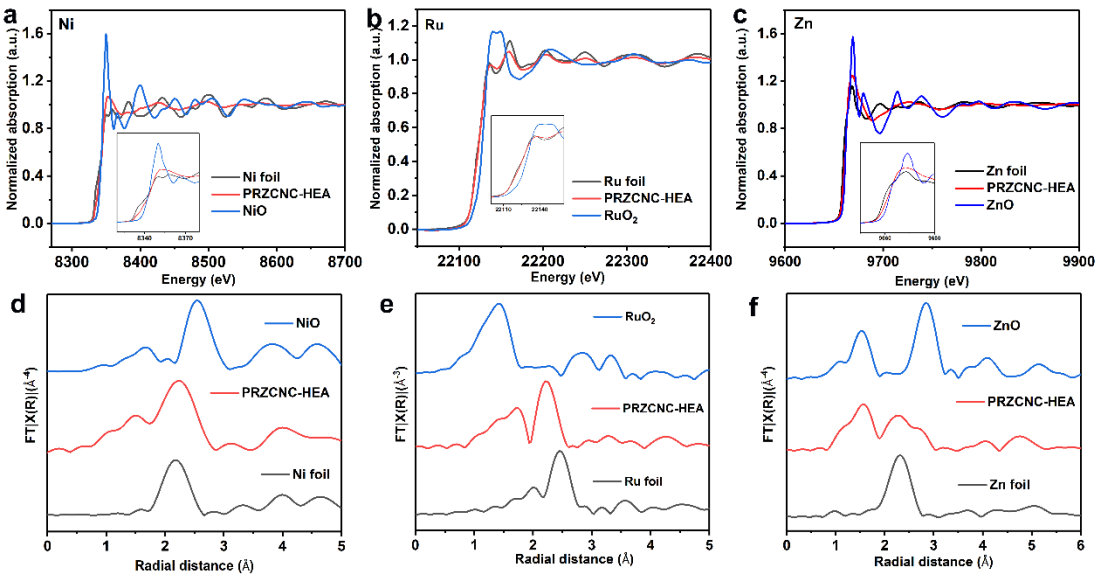

Figure S6. XANES spectra of (a) Ni, (b) Ru, and (c) Zn at the K-edge and EXAFS spectra of (d) Ni, (e) Ru, and (f) Zn for PRZCNC-HEA and corresponding reference samples.

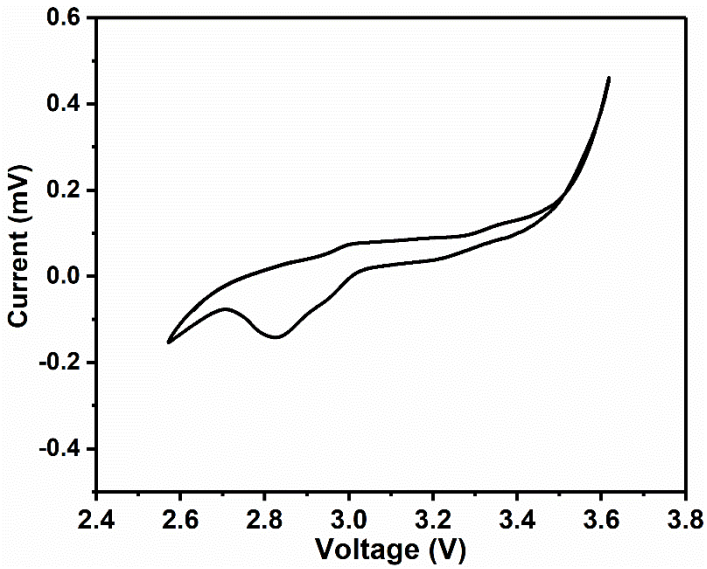

Figure S7. CV curve of Li–CO_2 battery with PRZCNC-HEA catalyst.

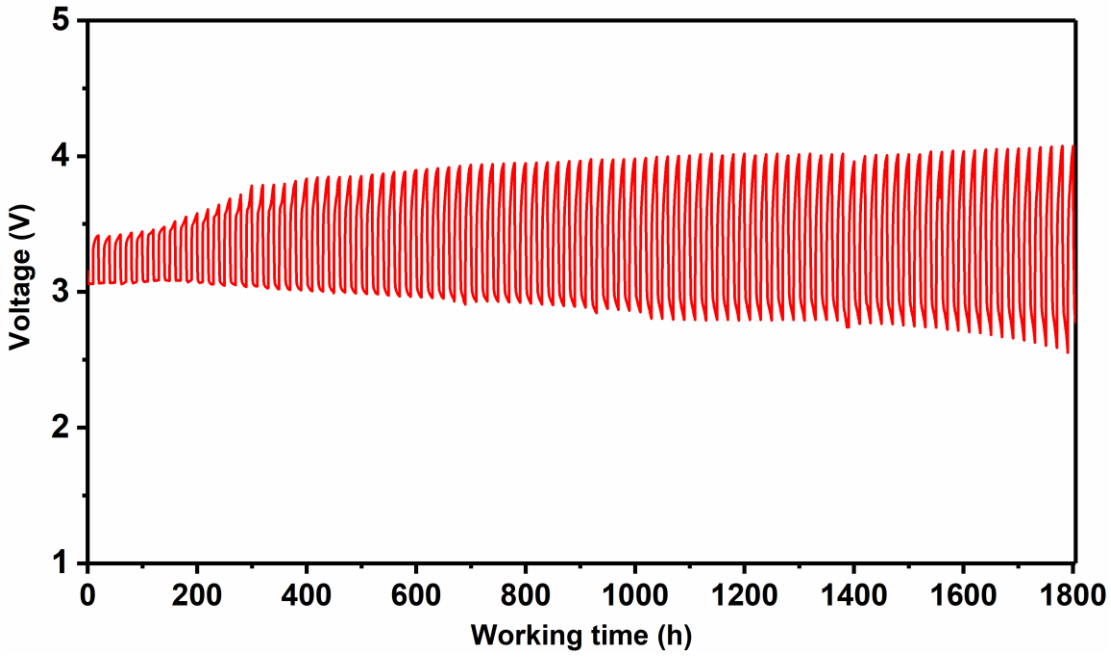

Figure S8. Time–voltage curve of PRZCNC-HEA at a current density of 100 mA g^{-1}.

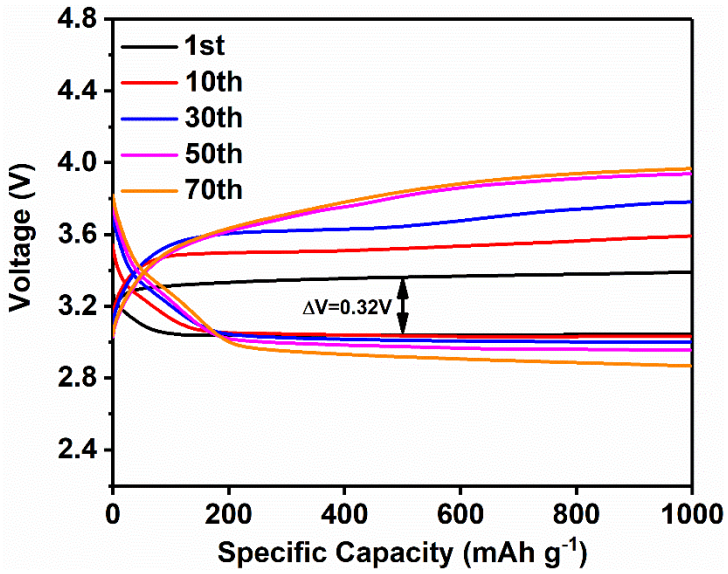

Figure S9. Charge–discharge curves of PRZCNC-HEA during various cycles at a current density of 100 mA g^{-1}.

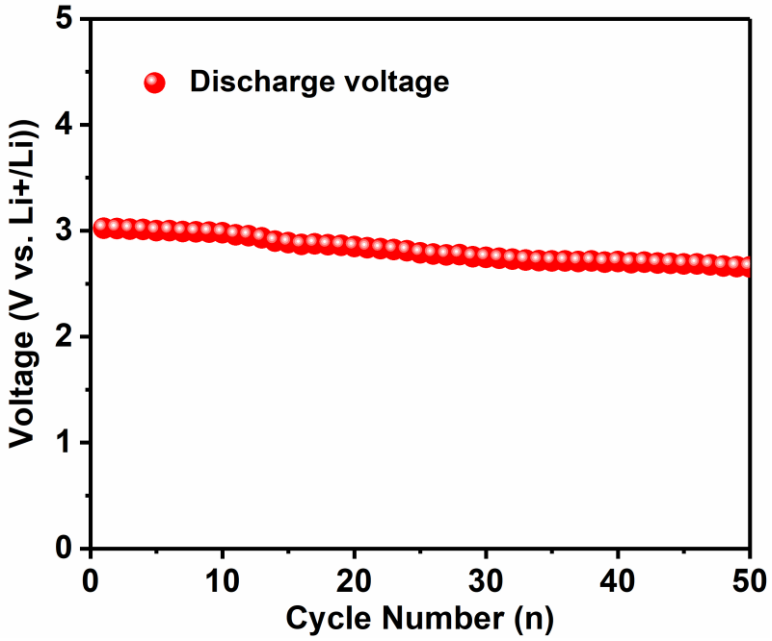

Figure S10. Cycling performance of PRZCNC-HEA at a cutoff capacity of 1000 mAh g^{-1} and current density of 200 mA g^{-1}.

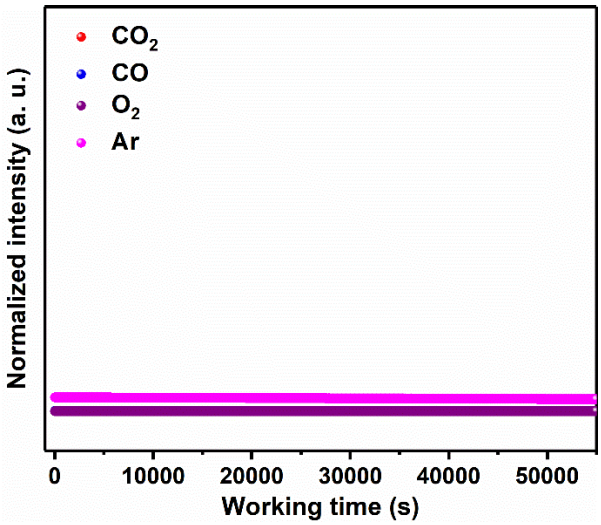

Figure S11. In situ DEMS results for the Li–CO_2 battery during the charging voltage interval, corresponding to the data shown in Figure 4e. The cathode of this battery consisted solely of carbon cloth without the PRZCNC-HEA catalyst, whereas the other components remained unchanged. The electrolyte was 1 M LiTFSI/TEGDME.

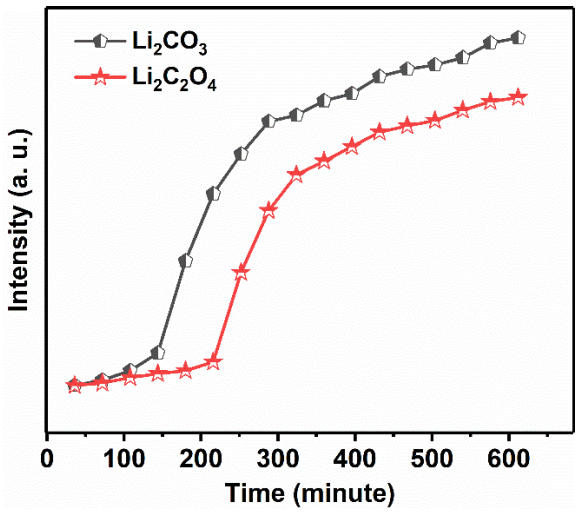

Figure S12. Temporal evolution of $Li_2C_2O_4$ and Li_2CO_3 peak intensities during in situ FTIR spectroscopy measurements.

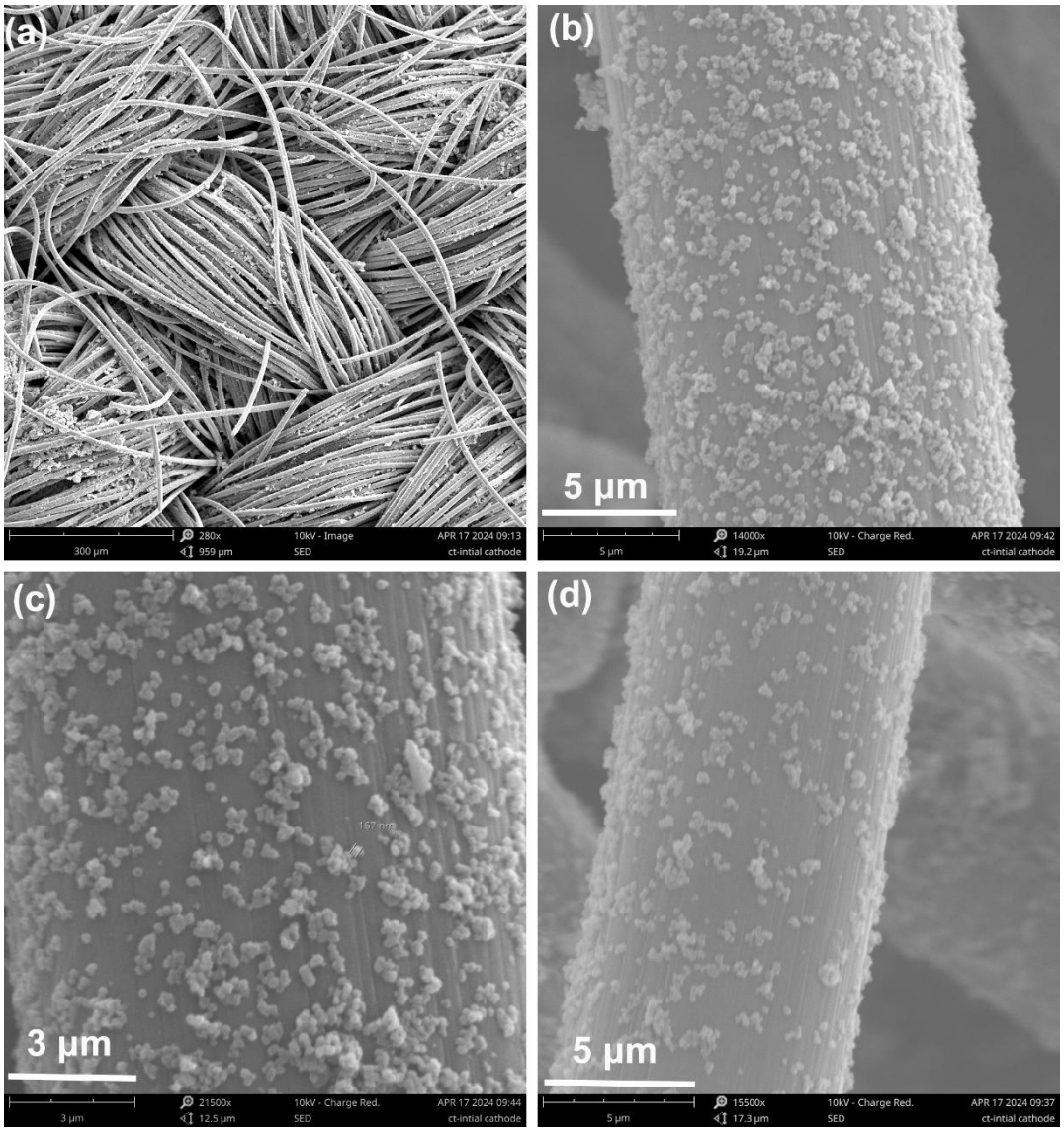

Figure S13. SEM images of pristine cathode.

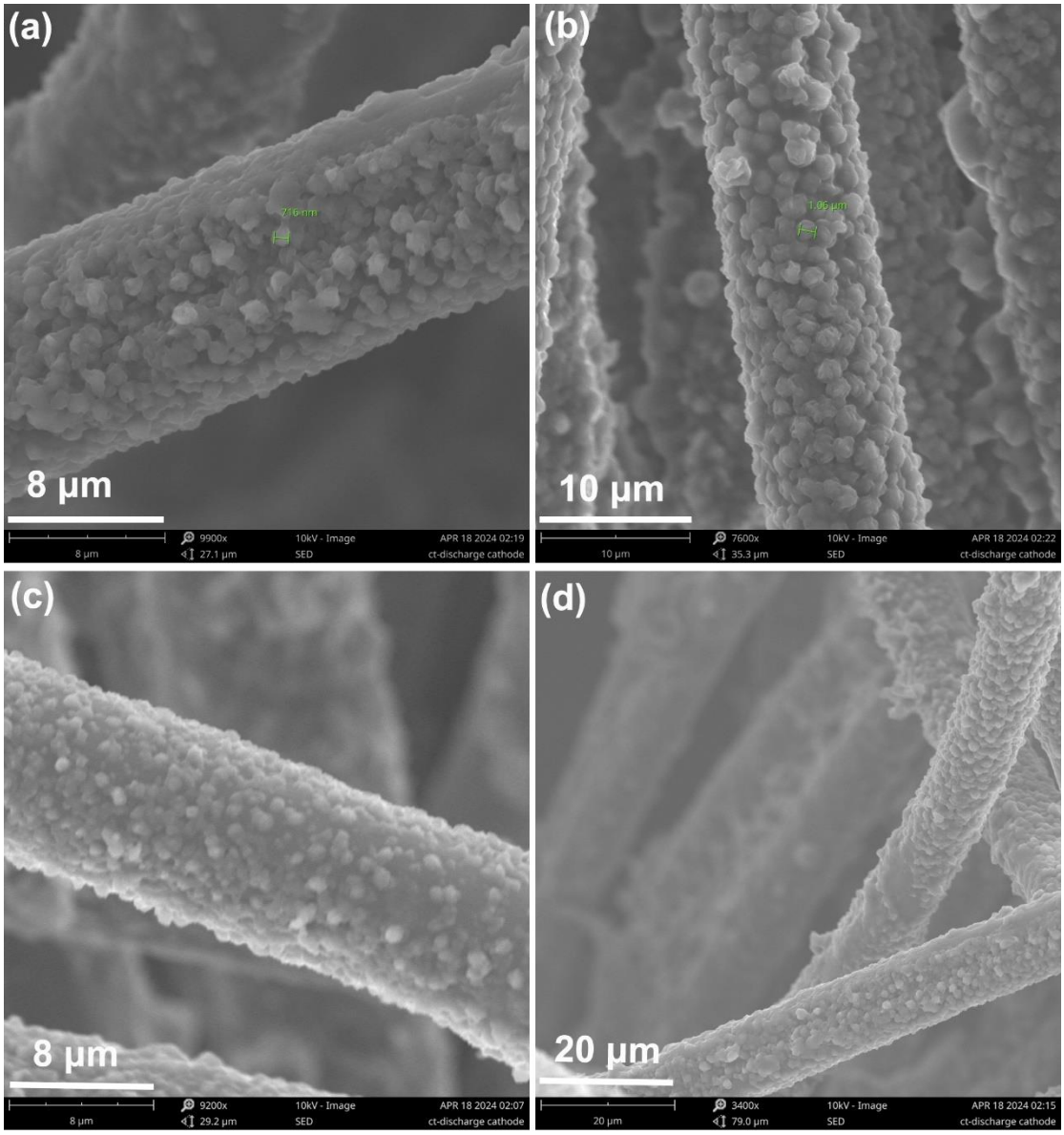

Figure S14. SEM images of cathode after discharge to 1000 mAh g^{-1}.

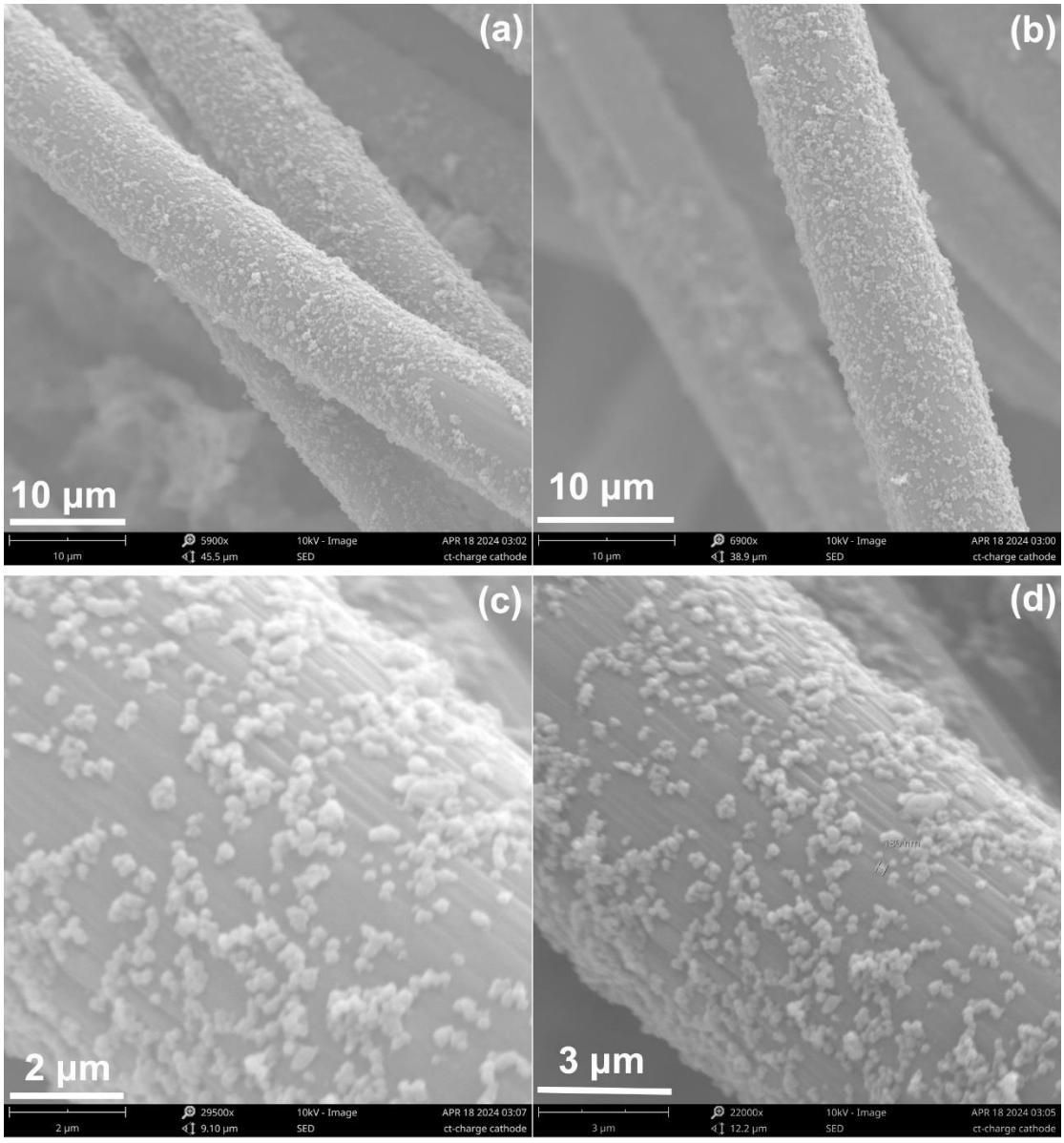

Figure S15. SEM images of cathode after charge to 1000 mAh g^{-1}.

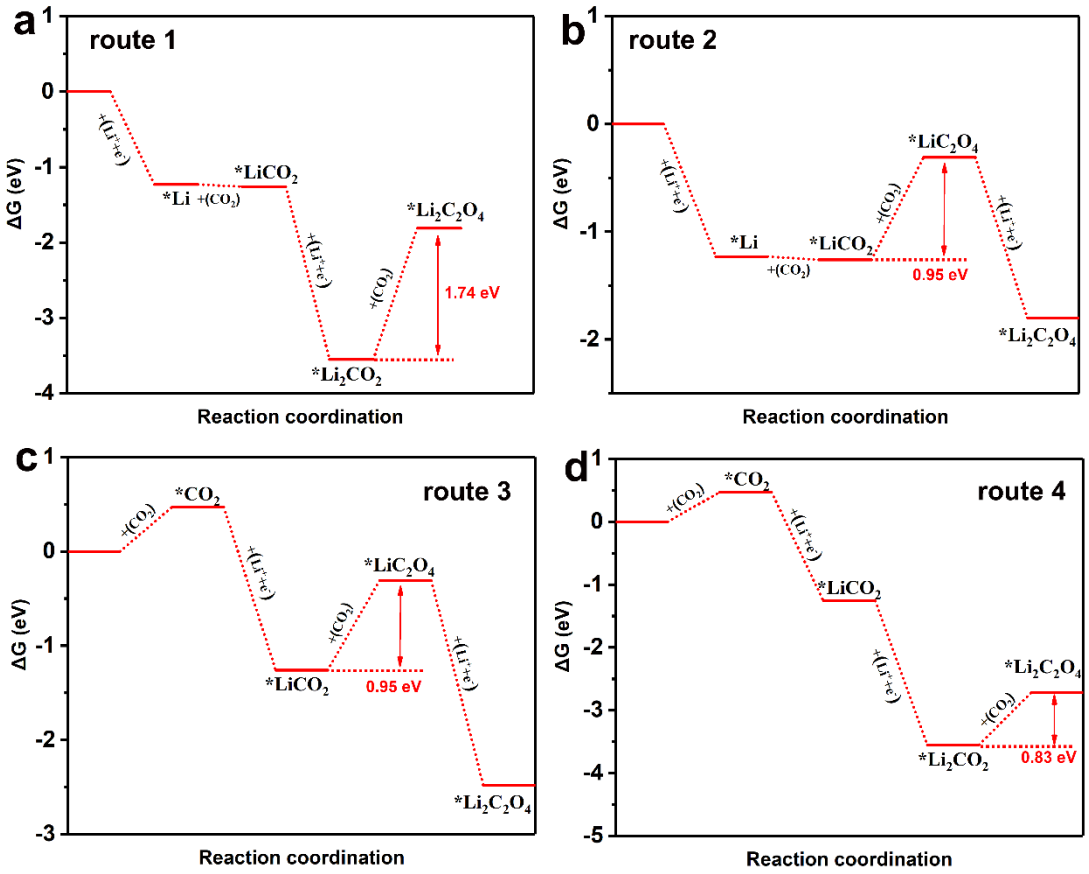

Figure S16. (a–d) Free energies of intermediates during CO_2 reduction to generate $Li_2C_2O_4$ via various pathways.

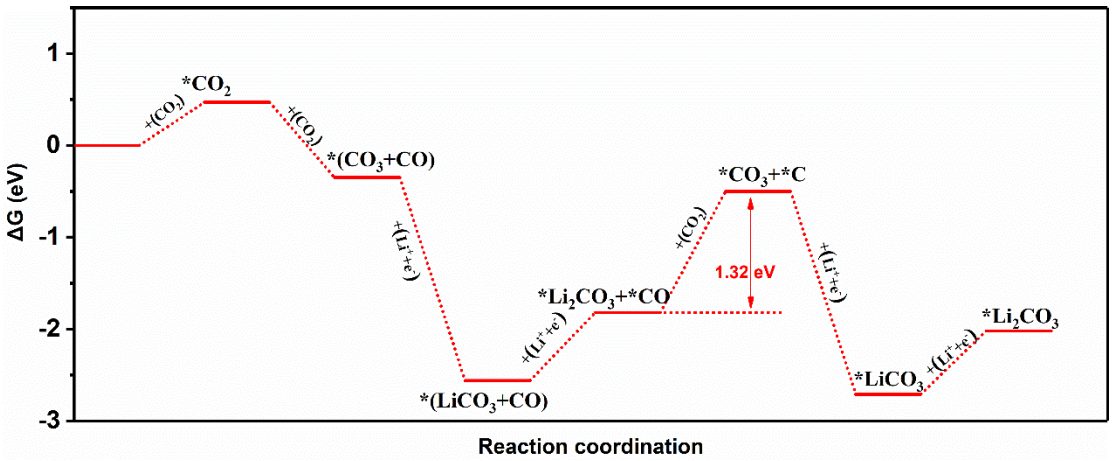

Figure S17. Free energies of intermediates during CO_2 reduction to generate Li_2CO_3 at Cu–CoCoRuRuZn sites on the PRZCNC-HEA surface, corresponding to pathway (5)′ in Supplementary Note 3.

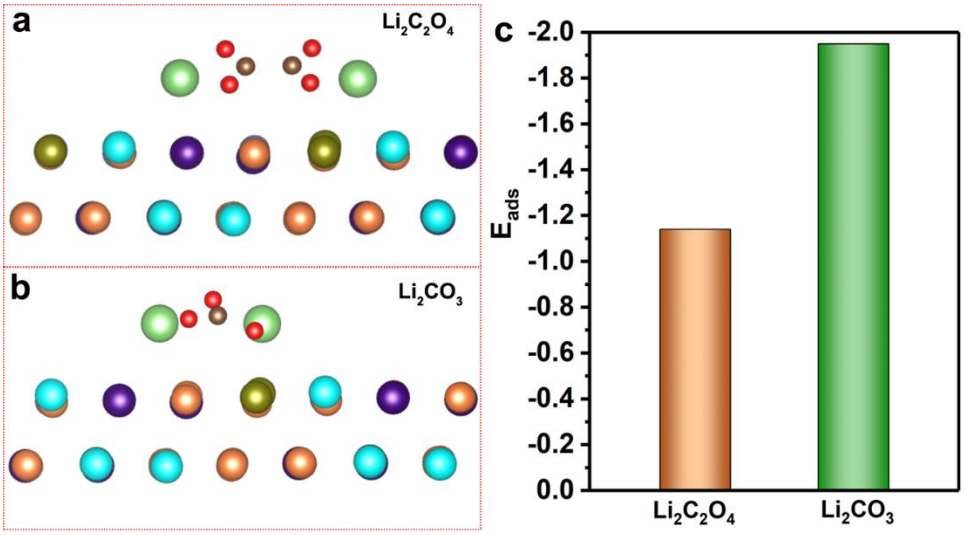

Figure S18. Adsorption states of (a) lithium oxalate and (b) lithium carbonate at Pt sites on the PRZCNC-HEA surface, and (c) corresponding adsorption energies.

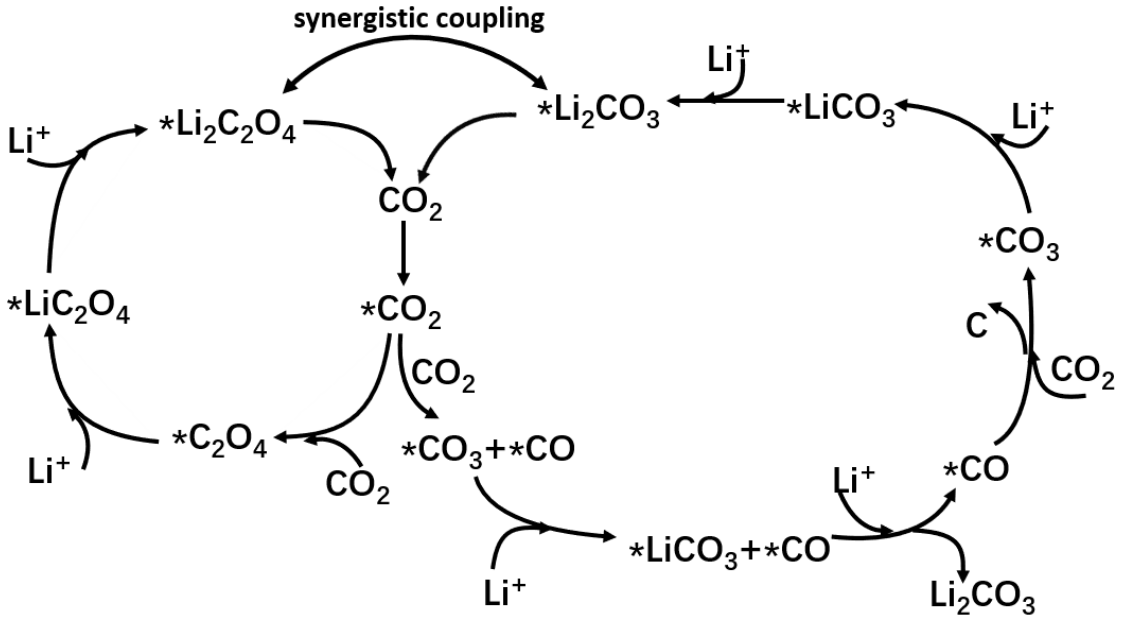

Figure S19. Simulated reaction pathway and intermediates for Li–CO_2 batteries during discharge with the PRZCNC-HEA catalyst.

Table S1. Performance comparison for PRZCNC-HEA and other reported Li–CO_2 battery cathode catalysts.

Catalyst	Discharge voltage (V)	Overpotential (V)	Discharge capacity (mAh g^{-1})	Energy efficiency	Reference
Ru_{AC+SA}@NCB	3.01	1.65	1000	73.6%	[1]
Co_2CuS_4	2.79	0.76	1900	78%	[2]
Ni/Ru HNPs	2.87	0.88	9700	76%	[3]
$Ru(bpy)_3Cl_2$	2.68	1.18	17750	70%	[4]
TDG-1000	2.8	1.12	Unknown	55.82%	[5]
MnOx-CeO_2@PPy	2.55	1.49	13631	63.1%	[6]
Ru@G	2.7	0.63	9000	76%	[7]
Fe-ISA/N,S-HG	2.78	1.17	23174	70.4%	[8]
ReS_2	2.6	0.66	Unknown	79.9%	[9]
PRZCNC-HEA	**3.06**	**0.32**	**12294**	**91%**	**This work**

Table S2. Lithium oxalate and lithium carbonate adsorption energies on various surface sites of PRZCNC-HEA.

Element site	Adsorption energy ($Li_2C_2O_4$, eV)	Adsorption energy (Li_2CO_3, eV)
Cu–CoCoRuRuZn	−1.41	−1.10
Pt–CuCuCoCoCuRu	−1.27	−1.53
Co–CuRuRuNiCuCo	−1.51	−1.57
Zn–NiPtCuCuRuCu	−1.28	−1.31
Ni–CoCuPtZnCuRu	−1.57	−1.41
Ru–CuRuCuNiCuPt	−1.14	−1.95

Supplementary Note 1

The thermal decomposition of ZIF-8 produced a porous metal–organic framework based on zinc metal and dodecahedral porous carbon nitride (Zn-DPCN), as shown in Figure S1. Using Zn-DPCN as a porous support, an ultrasmall PRZCNC-HEA catalyst was prepared via a spatial confinement strategy.

Supplementary Note 2

To investigate the stability of $Li_2C_2O_4$ and Li_2CO_3 nucleation on the HEA (111) surface, the adsorption energy was calculated using DFT optimization. The adsorption energy (E_{ad}) is defined as:

$$E_{ad}(M) = E_{total} - E_M - E_{slab} \quad (1)$$

where E_{total} is the total DFT energy of an adsorbate absorbed on the surface, E_M is the total energy of an isolated molecule, and E_{slab} is the total energy of the relaxed surface slab model.

The chemical reaction pathways were determined by calculating the standard Gibbs free energies. The zero-point energy, enthalpy, and entropy corrections of the adsorbates were calculated to convert the energy into free energy. The Gibbs free energy (G) of an isolated adsorbate was calculated using Equation (2):[10]

$$G = E_{total} + E_{zpe} - TS \quad (2)$$

where E_{zpe}, T, and S are the zero-point energy, temperature (298 K), and entropy, respectively. The entropy of CO_2 molecules under standard condition were obtained from the NIST database,[7] and the entropies of other adsorbates were calculated using DFT based on vibrational frequencies. The adsorption sites mentioned in this manuscript refer to the center coordinates of molecules on top of the HEA surface atoms. When modeling each reaction step, the intermediate product was derived by corelaxation of the product from the previous reaction step and the adsorbate from the next step. Each intermediate with the surface slab was modeled independently based on the calculation method proposed by Nørskov et al.[10,11]

Supplementary Note 3

Li_2CO_3 nucleation on PRZCNC-HEA can be initiated via the following five pathways:

$$PRZCNC\text{-}HEA + Li^+ + e^- \rightarrow *Li^+ + CO_2 \rightarrow *LiCO_2 + Li^+ + e^- \rightarrow *Li_2CO_2 + CO_2 \rightarrow *Li_2CO_3 + CO + CO_2 \rightarrow *CO_3 + C + Li^+ + e^- \rightarrow *LiCO_3 + C + Li^+ + e^- \rightarrow *Li_2CO_3 + C \quad (1)'$$

$$PRZCNC\text{-}HEA + Li^+ + e^- \rightarrow *Li^+ + CO_2 \rightarrow *LiCO_2 + CO_2 \rightarrow *LiCO_3 + CO + Li^+ + e^- \rightarrow *Li_2CO_3 + CO \rightarrow *CO_3 + C + Li^+ + e^- \rightarrow *LiCO_3 + C + Li^+ + e^- \rightarrow *Li_2CO_3 + C \quad (2)'$$

$$PRZCNC\text{-}HEA + CO_2 \rightarrow *CO_2 + Li^+ + e^- \rightarrow *LiCO_2 + Li^+ + e^- \rightarrow *Li_2CO_2 + CO_2 \rightarrow *Li_2CO_3 + CO \rightarrow *CO_3 + C + Li^+ + e^- \rightarrow *LiCO_3 + C + Li^+ + e^- \rightarrow *Li_2CO_3 + C \quad (3)'$$

$$PRZCNC\text{-}HEA + CO_2 \rightarrow *CO_2 + Li^+ + e^- \rightarrow *LiCO_2 + CO_2 \rightarrow *LiCO_3 + CO + Li^+ + e^- \rightarrow *Li_2CO_3 + CO \rightarrow *CO_3 + C + Li^+ + e^- \rightarrow *LiCO_3 + C + Li^+ + e^- \rightarrow *Li_2CO_3 + C \quad (4)'$$

$$PRZCNC\text{-}HEA + CO_2 \rightarrow *CO_2 + CO_2 \rightarrow *CO_3 + CO + Li^+ + e^- \rightarrow *LiCO_3 + CO + Li^+ + e^- \rightarrow *Li_2CO_3 + CO \rightarrow *CO_3 + C + Li^+ + e^- \rightarrow *LiCO_3 + C + Li^+ + e^- \rightarrow *Li_2CO_3 + C \quad (5)'$$

1. J. Lin, J. Ding, H. Wang, X. Yang, X. Zheng, Z. Huang, W. Song, J. Ding, X. Han and W. Hu, *Advanced Materials*, 2022, **34**, 2200559.
2. B. Lu, X. Wu, X. Xiao, B. Chen, W. Zeng, Y. Liu, Z. Lao, X. X. Zeng, G. Zhou and J. Yang, *Advanced Materials*, 2024, **36**, 2308889.
3. L. Fan, H. Shen, D. Ji, Y. Xing, L. Tao, Q. Sun and S. Guo, *Advanced Materials*, 2022, **34**, 2204134.
4. Z. Zhang, W. L. Bai, Z. P. Cai, J. H. Cheng, H. Y. Kuang, B. X. Dong, Y. B. Wang, K. X. Wang and J. S. Chen, *Angewandte Chemie International Edition*, 2021, **133**, 16540-16544.
5. A. Jaradat, M. K. Ncube, I. Papailias, N. Rai, K. Kumar, V. Koverga, R. Y. Nemade, C. Zhang, N. Shan and H. Shahbazi, *Advanced Energy Materials*, 2024, 2303467.
6. Q. Deng, Y. Yang, C. Mao, T. Wang, Z. Fang, W. Yan, K. Yin and Y. Zhang, *Advanced Energy Materials*, 2022, **12**, 2103667.
7. C. Guo, F. Zhang, X. Han, L. Zhang, Q. Hou, L. Gong, J. Wang, Z. Xia, J. Hao and K. Xie, *Advanced Materials*, 2023, **35**, 2302325.
8. C. Hu, L. Gong, Y. Xiao, Y. Yuan, N. M. Bedford, Z. Xia, L. Ma, T. Wu, Y. Lin and J. W. Connell, *Advanced Materials*, 2020, **32**, 1907436.
9. B. Chen, D. Wang, J. Tan, Y. Liu, M. Jiao, B. Liu, N. Zhao, X. Zou, G. Zhou and H. M. Cheng, *Journal of the American Chemical Society*, 2022, **144**, 3106-3116.